Inorganic Chemistry
Article
Cite This: *Inorg. Chem.* XXXX, XXX, XXX−XXX
pubs.acs.org/IC

$[(CH_3)_2NH_2]_7Pb_4X_{15}$ (X = Cl^- and Br^-), 2D-Perovskite Related Hybrids with Dielectric Transitions and Broadband Photoluminiscent Emission

Alberto García-Fernández,*[†] Juan Manuel Bermúdez-García,[†] Socorro Castro-García,[†] Antonio Luis Llamas-Saiz,[‡] Ramón Artiaga,[§] Jorge José López-Beceiro,[§] Manuel Sánchez-Andújar,*[†] and María Antonia Señarís-Rodríguez[†]

[†]QuiMolMat Group, Department of Chemistry, Faculty of Science and CICA, University of A Coruña, Campus A Coruña, 15071 A Coruña, Spain

[‡]RIAIDT X-ray Unit, University of Santiago de Compostela, 15782 Santiago de Compostela, Spain

[§]Department of Industrial Engineering II, University of A Coruña, Campus Ferrol, 15403 Ferrol, Spain

Supporting Information

ABSTRACT: We have prepared two new lead halides with the novel general formula of $DMA_7Pb_4X_{15}$ (DMA = $[(CH_3)_2NH_2]^+$ and X = Cl^- or Br^-) by using an easy route under mild conditions at room temperature. These compounds exhibit an unprecedented crystal structure, are formed by layers of distorted $[PbX_6]$ octahedra, which share corners and faces, and contain intercalated DMA cations. Very interestingly, they display dielectric transitions, which are related to a partial order−disorder process of the DMA cations between 160 and 260 K. Additionally, these new layered hybrids exhibit a broadband photoluminiscent emission, which is related to the structural distortions of the $[PbX_6]$ octahedra. These findings not only open up large possibilities for future optoelectronic applications of these materials, but they also offer a novel playground for an easy modulation of electrical and optical properties of hybrid organic−inorganic materials. We anticipate that this novel $A_7Pb_4X_{15}$ formula can be adequate to tune the family of the hybrid lead halides using other alkylammonium cations, such as methylammonium, formamidinium, or ethylammonium, to improve their photoelectronic properties.

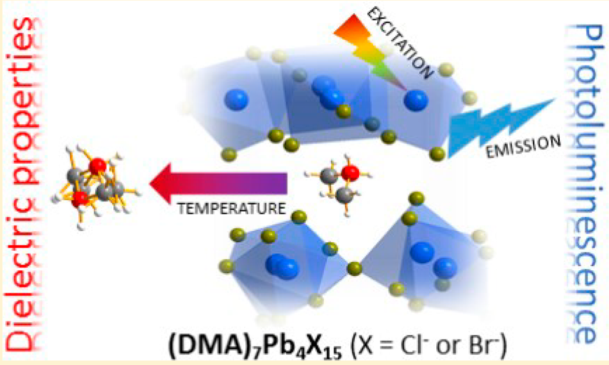

■ INTRODUCTION

In the past years, lead halide materials with hybrid organic−inorganic components have received much attention due to the discovery of the unprecedented photovoltaic and optoelectronic properties in $APbX_3$ compounds with a perovskite structure,[1−6] where A= Cs^+, $[CH_3NH_3]^+$ (methylammonium, MA) and/or $[HC(NH_2)_2]^+$ (formamidinium, FA) and X = Cl^-, Br^-, and/or I^-.[7,8]

Owing to the flexibility and ease of manipulation of such a perovskite structure, many substitutions have been explored in the search for optimized materials.[9,10] In addressing materials beyond hybrid halide $APbX_3$ perovskite, the A cation (MA and FA) has been replaced by larger organic cations.[11,12] This replacement often makes the 3D perovskite structure no longer favorable, while the lower-dimensional structures become more stable. This decrease of the dimensionality from 3D to 2D is in general an interesting strategy to tune the electronic and optical properties of materials.[13,14] In addition, very versatile organic cations can be incorporated to obtain new crystal structures.[15,16] Moreover, longer organic cations are typically hydrophobic, which avoids one of the main drawbacks of the perovskite lead halides, their instability toward moisture.[17,18] Hence, 2D lead halides usually show better chemical stability than the 3D perovskite materials.[19,20]

It is worth highlighting that the organic cations and the anionic inorganic framework have a templating influence on each other, allowing a certain degree of control over the final structures and properties.[21,22] The choice of the organic cation(s) and the stoichiometry of the reaction are among the most influential parameters on the orientation and deformation of the resultant inorganic frameworks.[23] In that context, in most of the known low-dimensional lead halide perovskites, the organic cation A must contain terminal functional groups that can ionically interact with the anionic inorganic framework, such as mono- or di-ammonium cations of general formula $(RNH_3)^+$ or $(NH_3RNH_3)^{2+}$,[24] where R represents an organic functional group. The framework is based

Received: December 27, 2017

DOI: 10.1021/acs.inorgchem.7b03217

on one layer or several layers of corner-sharing [PbX_6] octahedra. The most common low-dimensional perovskite derivatives display the following general formula: $(RNH_3)_2A_{n-1}Pb_nX_{3n+1}$,[25] $A'_2A_mPb_mX_{3m+2}$,[26] and $A'_2A_{q-1}Pb_qX_{3q+3}$.[11]

A property recently discovered in these 2D-hybrid perovskites is their broadband light emission;[27−30] this makes them interesting as broadband phosphors, for applications as artificial illumination or the manufacturing of displays, among others. While most broadband inorganic phosphors must contain emissive extrinsic dopants or surface defect sites, the broad photoluminescence (PL) of those 2D-hybrid perovskites is supposed to be due to self-trapped excitons, STEs (i.e., excited electron-hole pairs stabilized though coupling to a deformable lattice).[31,32] Therefore, the emission in those layered perovskites could be amenable with a fine synthetic tuning.[15] In this context, it has been recently reported that a distortion of the [PbX_6] octahedra has an important role on the PL emission of different 2D-lead halides.[13,23,33−36]

On the other hand, the 2D-hybrid perovskites of general formula A_2MX_4 (A= organic cation, M metal ions, and X = halide) constitute a large family of organic−inorganic hybrids with well-known interesting ferroelectric (FE) properties, this made them interesting for applications as a capacitor and FE random-access memory (RAM), among others.[37] In those systems, the organic cations, A, located in the anionic cavities are believed to be responsible for the ferroelectric ordering in most cases. Also, it has been shown that the dimethylammonium $[(CH_3)_2NH_2]^+$ (DMA) cations can experience thermally induced order−disorder processes in several hybrid perovskites, giving rise to structural phase transitions with associated interesting properties.[38−41] Very recently, we reported a first-order phase transition and a dielectric transition at around 250 K in a $[(CH_3)_2NH_2]PbI_3$ 2H-hexagonal perovskite.[42]

All of these results suggest that the substitution of the halide in the $DMAPbI_3$ compound, together with changes in its stoichiometry, can offer new possibilities to achieve novel hybrid lead halide perovskites with interesting dielectric and photophysical properties.

In this context, in this work, we report the synthesis of two new hybrid lead halides designed by combining the possibilities offered by a framework based on more or less distorted [PbX_6] octahedra with a peculiar connectivity and DMA guests prone to experience order−disorder transitions. As we will show, the obtained compounds, which display a new and original structure and formula, $(DMA)_7Pb_4X_{15}$, where X= Cl^- and Br^-, have been characterized in depth by single-crystal-X-ray diffraction (SCXRD), thermogravimetric analysis (TGA), and differential scanning calorimetry (DSC). Their dielectric and optical (optical diffuse−reflectance and emission spectra) characterizations reveal that these materials display dielectric transitions below room temperature, and a broadband photoluminiscent emission at room temperature.

■ EXPERIMENTAL SECTION

Materials. All starting materials were of analytical grade from commercial sources, with the exception of the $(CH_3)_2NH_2Br$. $(CH_3)_2NH_2Cl$ (99%) (DMACl), $(CH_3)_2NH$ solution (40 wt % in H_2O), $PbCl_2$ (99%), $PbBr_2$ (99%), HCl solution (37 wt % in H_2O), and HBr solution (48 wt % in H_2O) were purchased from Sigma-Aldrich and used without further treatment.

Synthesis of $(CH_3)_2NH_2Br$ (DMABr). Dimethylamine $(CH_3)_2NH$ solution in a slight excess was reacted with hydrobromic acid (HBr) in an ice bath. The crystallization of dimethylammonium bromide ($(CH_3)_2NH_3Br$) was achieved using a rotary evaporator; a white colored powder was formed indicating successful crystallization. The white microcrystals of $(CH_3)_2NH_3Br$ were washed with absolute diethyl ether several times and finally dried under vacuum overnight.

Synthesis of $[(CH_3)_2NH_2]_7Pb_4X_{15}$ (X= Cl^- and Br^-). Single-crystals of both $DMA_7Pb_4X_{15}$ have been obtained by crystallization from a *N*,*N*-dimethylformamide (DMF) solution. For this purpose, stoichiometric amounts of PbX_2 (X = Cl or Br) (4 mmol) and of DMAX (X = Cl or Br) (7 mmol) were dissolved by adding 5 mL of DMF. The obtained solution was filtered through a 0.45 μm PTFE filter to minimize nucleation sites. Colorless, needle-shaped single-crystals of $DMA_7Pb_4Cl_{15}$ and colorless, cubic single-crystals of $DMA_7Pb_4Br_{15}$ were obtained upon slow evaporation of the solvent at room temperature after several days.

Additionally, powder of $[(CH_3)_2NH_2]_7Pb_4X_{15}$ (X= Cl^- and Br^-) compounds were easily obtained by a solid state reaction at room temperature. For that purpose, 4 mmol of PbX_2 (X = Cl or Br) and 7 mmol of DMAX (X = Cl or Br) were placed in an agate mortar and ground carefully with a pestle until a visually homogeneous white powder was obtained.

Thermal Analysis. Thermogravimetric analysis (TGA) were carried out using TGA-DTA Thermal Analysis SDT2960 equipment. For these experiments, approximately 27 mg of grounded single crystals were heated at a rate of 5 K/min from 300 to 1200 K using corundum crucibles under a flow of dry nitrogen.

Differential scanning calorimetric (DSC) analyses were carried out in TA Instruments MDSC Q-2000 equipped with a liquid nitrogen cooling system by heating and cooling the samples during several cycles at 10 K/min from 160 up to 300 K under a nitrogen atmosphere.

Powder X-ray Diffraction. Powder X-ray diffraction (PXRD) patterns were collected in a Siemens D-5000 diffractometer using Cu Kα radiation at room temperature. The PXRD patterns were analyzed by the Le Bail method using GSAS+EXPGUI software.[43,44]

Single Crystal X-ray Diffraction. Single-crystal data sets were collected at different temperatures (275 and 100 K) in a Bruker Kappa X-ray diffractometer equipped with an Apex II CCD detector and using monochromatic Mo Kα radiation (λ = 0.71073 Å). A suitable crystal for each compound was chosen and mounted on a glass fiber using a two components epoxy glue (Araldit 7070, Ceys) for the Cl compound, and on a MiTeGen MicroMountTM using Paratone N (Hampton Research) for the Br compound. To carry out these experiments, the crystals were cooled at different rates using a nitrogen gas cold stream from an Oxford Cryosystems cooler (700 Series). The presence of multiple lattices was clear from visual inspection of diffraction images collected at 275 K for both crystals. Both data sets, at 275 K, were indexed using CELL_NOW 2008/4, and obtained two solutions that interpreted all the diffraction peaks, with $I/\sigma(I) > 8$ found in the 1337 and 2855 images measured for the Cl and Br compounds, respectively. The data integration, reduction, and correction for Lorentz and polarization effects were performed using SAINT V8.37A included in the APEX2 V2015.9-0 (Bruker AXS, 2015) suite of software. The integration of the reflections for all data sets were performed taking into account the orientation matrices of the two twin domains simultaneously. The reflection intensities were corrected for absorption effects by semiempirical methods on the basis of symmetry-equivalent data using TWINABS 2012/1 included in the Bruker software suite.

The structures were solved by direct methods using the SHELXT2014/5[45] program and were refined by least-squares methods on SHELXL2014/7. To refine the structures, anisotropic thermal factors were employed for the non-H atoms. The hydrogen atoms of the NH_2^+ group of the DMA cations could be found in the Fourier maps, and the rest of the hydrogen atoms of the DMA were introduced at idealized positions. All hydrogen atoms were restrained using the riding model implemented in SHELXL2014/7.

Dielectric Properties. The complex dielectric permittivity ($\varepsilon_r = \varepsilon'_r - i\varepsilon''_r$) of the cold-press pelletized samples was measured as a function of frequency and temperature with a parallel-plate capacitor coupled to a Solartron 1260A impedance/gain-phase analyzer, capable of measuring in the frequency range from 10 μHz up to 32 MHz using an amplitude of 2 V. The capacitor was mounted in a Janis SVT200T cryostat refrigerated with liquid nitrogen, and with a Lakeshore 332 incorporated to control the temperature from 100 up to 350 K. The data were collected on heating, and before carrying out the measurements, the pellets were kept for 2 min at each temperature so as to reach the thermal equilibrium.

Pelletized samples, made out of cold-press grounded single-crystals, with an area of approximately 530 mm^2 and a thickness of approximately 0.7 mm were prepared to fit into the capacitor. Gold was sputtered on the surfaces of the pelletized samples to ensure a good electrical contact.

All the dielectric measurements were carried out in a nitrogen atmosphere where several cycles of vacuum and nitrogen gas were performed to ensure that the sample environment was free of water.

Ultraviolet−Visible (UV−vis) Spectroscopy. Optical diffuse−reflectance measurements of grounded single-crystals were performed at room temperature using a Jasco V-730 UV−visible double-beam spectrophotometer with single monochromator, operating from 200 to 900 nm. $BaSO_4$ was used as a nonabsorbing reflectance reference. The generated reflectance-versus-wavelength data were used to estimate the band gap of the material by converting reflectance to absorbance data according to the Kubelka−Munk equation:[46] $F(R)= \alpha = (1 - R)^2/2R$, where R is the reflectance data and α is the absorption coefficient.

Emission spectra were measured on a Horiba FluoroMax Plus-P spectrofluorometer equipped with a 150 W ozone-free xenon arc lamp and a R928P photon counting emission detector, as well as a photodiode reference detector for monitoring lamp output. Samples were excited using a 150 W xenon arc lamp at 320 nm, and then the emission was measured from 400 to 700 nm.

The chromaticity coordinates were calculated using the Color-Calculator by OSRAM Sylvania, Inc.[47] and plotted using the 1931 color space chromaticity diagram.

RESULTS AND DISCUSSION

Synthesis and Basic Characterization. For the first time, we have prepared two new compounds with the novel composition of $DMA_7Pb_4X_{15}$ (X = Cl or Br) by using an easy route under mild conditions at room temperature.

These compounds were obtained not only as single crystals but also as powdered samples by using a mechanosynthesis method. In this context, it is worth noting that we have tried to prepare the iodide compound, but we did not succeed and we have always obtained the $DMAPbI_3$ hexagonal perovskite phase instead of the desired compound.

We have confirmed the purity of the so-prepared samples by Le Bail refinements of their PXRD data collected at room temperature, which show good agreement between the experimental data and the model. The new $DMA_7Pb_4Cl_{15}$ structure displays orthorhombic symmetry, with cell parameters of a = 18.8778(4) Å, b = 15.9548(3) Å, and c = 32.0809(7) Å and space group Pbca (Figure S1). Meanwhile the structure of the $DMA_7Pb_4Br_{15}$ compound exhibits monoclinic symmetry, with a = 17.0859(3) Å, b = 19.6358(3) Å, c = 16.4307(3) Å, and β = 105.7190(10) and space group $P2_1/c$ (Figure S2). As we will show below, the so-obtained cell parameters and space groups are in agreement with those obtained by single-crystal X-ray diffraction (see below).

Interestingly, we have observed that both compounds are stable in air at room temperature for several months, and their X-ray diffraction patterns remain unchanged after this period.

As for their thermal stability, according to our TGA results (Figure S3), these compounds are stable up to ∼450 K (Cl) and up to ∼470 K (Br).

Differential Scanning Calorimetry (DSC). The differential scanning calorimetry analysis of grounded single crystals (Figure. 1) shows that both compounds exhibit endothermic (on heating) and exothermic (on cooling) peaks, in the temperature range of 160−300 K, probably due to one or several phase transitions. Nevertheless, both compounds display slightly different behaviors, while $DMA_7Pb_4Cl_{15}$ presents a single acute endothermic peak on heating at around 262 K (and the corresponding exothermic peak on cooling at around 256 K), $DMA_7Pb_4Br_{15}$ exhibits three weak endothermic peaks, two broad peaks at ∼182 and ∼202 K and an acute peak at ∼252 K (with the corresponding exothermic peaks at ∼178, ∼ 198, and ∼248 K).

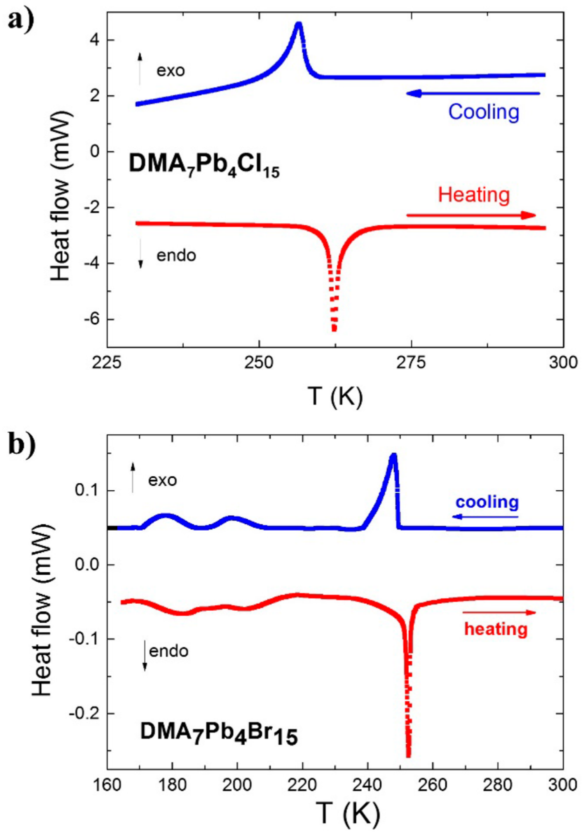

Figure 1. DSC results as a function of temperature obtained by heating and cooling the samples (a) $DMA_7Pb_4Cl_{15}$ and (b) $DMA_7Pb_4Br_{15}$ at a rate of 10 K min^{-1}.

The changes in the enthalpy ΔH (J/mol) and the entropy ΔS (J/mol K) were determined from the area under the peaks of the heat flow curves. The results yield $\Delta H \sim$ 2984 J/mol (endo) − 3536 J/mol (exo) and $\Delta S \sim$ 11.38 J/mol (endo) − 13.48 J/mol (exo) K for the Cl compound, and $\Delta H \sim$ 173.08 J/mol (endo) − 269.31 J/mol (exo) and a $\Delta S \sim$ 0.68 J/(mol K) (endo) − 1.07 J/(mol K) (exo) for Br compound (only considering the high temperature).

This DSC behavior is reminiscent of that shown by other perovskite systems containing DMA cations, such as $DMAMn(HCOO)_3$[48] and $DMAPbI_3$,[42] which exhibit structural transitions associated with order−disorder processes of DMA cations. Using these studies as a reference, we have evaluated a possible order−disorder process in our systems by using the calculated entropy. In that context, for an order−disorder transition, entropy is related with N (the ratio of the number of configurations in the disordered and ordered systems) by using the expression $\Delta S = R \ln(N)$, where R is the gas constant. Such an estimation leads to quite different N-values for the here studied Cl and Br compounds, 4 and 1, respectively. Therefore, even if the DSC results point to an order−disorder mechanism of the DMA cations, the $DMA_7Pb_4Br_{15}$ compound shows some particularities compared to the Cl analogous and to other reported hybrids, such as lower values of ΔH and ΔS and multiphase transitions.[49] These differences can be due to the extent of the order−disorder process, which takes place in steps and along a wider temperature range in the case of the Br compound.

Crystal Structure by Single-Crystal X-ray Diffraction. Single-crystal X-ray diffraction experiments were carried out at temperatures well above and below the observed DSC transitions, namely at 275 and 100 K. The space groups found corroborate the PXRD results reported above, giving *Pbca* for $DMA_7Pb_4Cl_{15}$ and $P2_1/c$ for $DMA_7Pb_4Br_{15}$. The crystallographic data of these two compounds are compiled in Table S1 and S2 of the SI The unit cell parameters of both compounds were analyzed and the following relationships were observed, a (Br) ∼ $c/2$ (Cl), b (Br) ∼ a (Cl), and c (Br) ∼ b (Cl). Also, it was observed that the cell parameters of the Cl compound are slightly lower than these of the Br compound, which is related with the smaller size of the chloride anions.

It is worth commenting that differences with the case of other hybrids,[38−42] such space groups, do not change as a function of temperature in the temperature range studied.

Another aspect that is worthwhile to highlighting is that, despite the fact that both compounds crystallize under different space groups, they display similar crystal structures that, very interestingly, are novel and different from any other crystal structure reported so far for lead halides.

Both structures consist on single-layered lead halide frameworks with intercalated DMA cations (Figure 2). Their asymmetric unit contains four independent Pb^{2+} cations, 15 X^- anions bounded to the metal cations, and seven DMA cations. The Pb^{2+} cations are in octahedral coordination with six halide ligands. The four $[PbX_6]^{4-}$ octahedra of the asymmetric unit are forming a linear $[Pb_4X_{15}]^{7-}$ chain, where two central $[PbX_6]^{4-}$ octahedra are sharing one corner, and they are linked to the terminal $[PbX_6]^{4-}$ octahedra by face-sharing. Additionally, each $[Pb_4X_{15}]^{7-}$ unit is sharing four corners with neighboring $[Pb_4X_{15}]^{7-}$ moieties (Figure 3), forming a layered structure. Six DMA cations per asymmetric unit are located between the layers, while one DMA cation occupies a cavity within the layer. The DMA cations are linked by H-bonds to the halide anions of the framework (Figure S4).

It is worthwhile to highlight another two interesting features of the structure:

(1) The fact that all $[PbX_6]^{4-}$ octahedra of the framework display a high distortion, with Pb-X bond lengths ranging, at 100 K, from 2.633(7) to 3.297(7) Å for the chloride compound, and from 2.779(3) to 3.290(3) Å for the bromide compound, with $\text{Pb-X}_{\text{terminal}}$ shorter than $\text{Pb-X}_{\text{bridging}}$ (Tables S1, S2, and S3).

(2) Another important feature concerns the DMA cations of the structure, which at T = 100 K are ordered, with all the C- and N-atoms sitting in a single crystallographic position (Figure 2). Nevertheless, at 275 K a certain disorder is observed (Figure S5) on the DMA cations located inside and close to the cavities of the framework, with all atoms located in two different positions. This disorder is also higher in the case of the Cl-compound with three of the DMA cations disordered per formula, while the Br-compound displays only two disordered DMA cations per formula. Therefore, we confirm by SCXRD that both compounds exhibit a partial order−disorder process of the DMA cations, which takes place to a larger extent in the Cl-compound, with the DMA

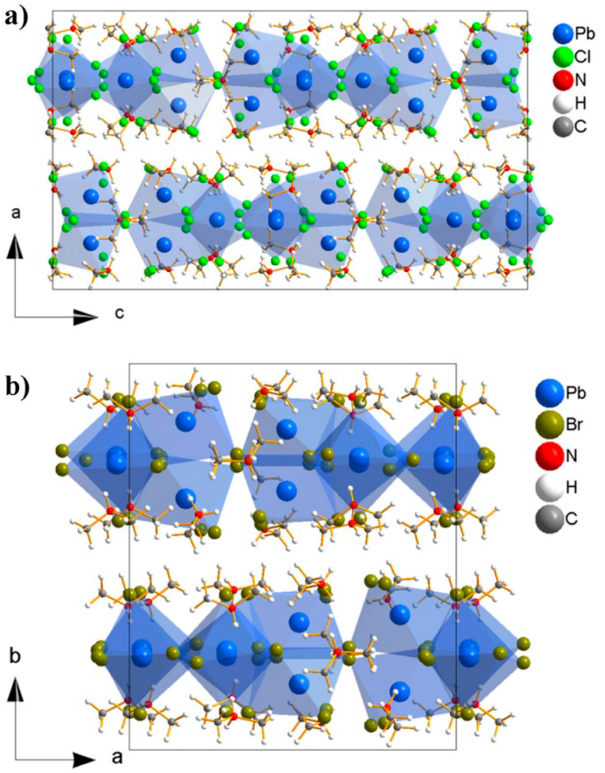

Figure 2. (a) View of the crystal structure of the $DMA_7Pb_4Cl_{15}$ compound at T = 100 K along the b-axis. (b) View of the crystal structure of the $DMA_7Pb_4Br_{15}$ compound at T = 100 K along the c-axis. As it can be seen, the DMA cations are cooperatively ordered in both structures.

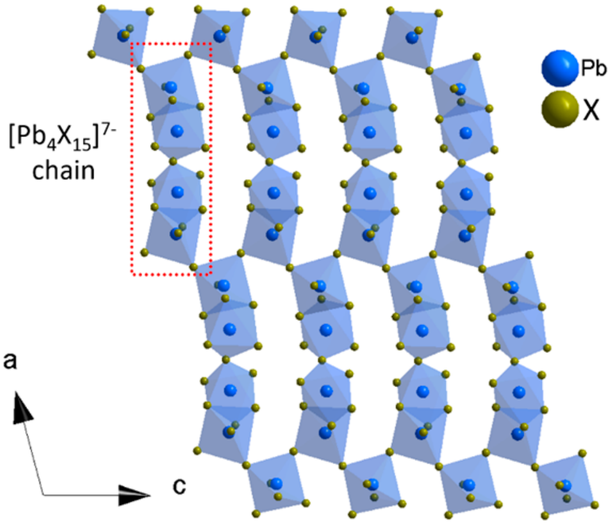

Figure 3. Details of the crystal structure of $DMA_7Pb_4X_{15}$ compounds, where the 2D arrangement of the framework is shown. The linear $[Pb_4X_{15}]^{7-}$ chain is highlighted inside a dot line.

DOI: 10.1021/acs.inorgchem.7b03217
Inorg. Chem. XXXX, XXX, XXX−XXX

cations fully ordered at T = 100 K, and a coexistence of ordered and disordered DMA cations at T= 275 K.

Dielectric Properties. The dielectric properties of the $DMA_7Pb_4X_{15}$ samples were studied in the range of temperatures where the structural phase transitions were observed by DSC. Figure 4 shows the temperature dependence of the real part of their complex dielectric permittivity (also known as dielectric constant, ε'_r) at different frequencies. The first general observation is that the values of ε'_r of both compounds are strongly temperature dependent, while they are independent of frequency. This behavior is similar to that previously reported for the 1D lead iodide $DMAPbI_3$ 2H-hexagonal polytype[42] and ascribed to the above-mentioned thermally activated order−disorder processes of the DMA cations. Nevertheless, there are significant differences in the dielectric behavior of both compounds. As it can be seen in Figure 4a, while in the Cl hybrid, the initial increase in ε'_r is followed by a sharp kink at about 270 K; in the case of the Br compound (Figure 4b), ε'_r shows a broad dielectric anomaly over a larger temperature range, which takes place already at lower temperatures, between 160 and 200 K.

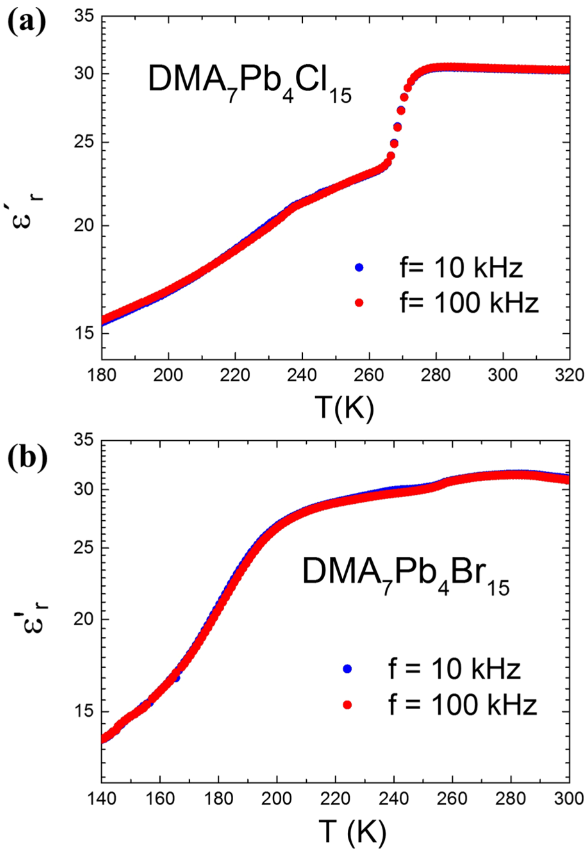

Figure 4. Temperature dependence of the dielectric constant (ε'_r) measured at different frequencies (10−100 kHz) for (a) $DMA_7Pb_4Cl_{15}$ and (b) $DMA_7Pb_4Br_{15}$.

UV−Visible Spectroscopy. In order to check the optoelectronic properties of the new compounds, we have evaluated their optical absorption. The optical spectra were measured in diffuse reflection mode by UV−visible spectrophotometry, and the corresponding results are shown in Figure 5. Absorption cutoff wavelengths of ~425 and ~350 nm were observed for the bromide and chloride hybrids, respectively. Additionally, the Br-compound has clear excitonic features near the absorption edge, as indicated by the shoulder found around 400 nm in the absorbance spectrum, and comparable to the feature exhibited by other 2D semiconductors.[18,36] The optical band gaps were calculated using the Kubelka−Munk equation, and values of 3.5 and 2.8 eV were obtained for the Cl- and the Br-compound, respectively. These values are also similar to those reported for other related 2D lead halides.[23] Thus, the obtained band gap of the chloride hybrid is ~0.7 eV larger than that of the bromide one, always in accordance with the values found for comparable hybrid lead halide compounds.[50,51]

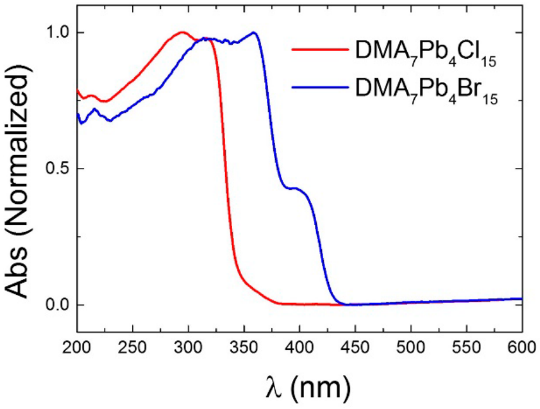

Figure 5. Optical absorption spectra of $DMA_7Pb_4X_{15}$ (X = Cl (red) and Br (blue)) at room temperature.

Moreover, the solid steady-state photoluminescence (PL) spectra were measured at room temperature (see Figure 6a). Both compounds display PL emission in the blue-light region (see below the chromaticity coordinates).

The results obtained here are in agreement with the commented literature,[13,23,33−36] which predicts the broadband photoluminiscent emission at room temperature for those 2D lead halides, related with the $[PbX_6]$ octahedra distortions.

Surprisingly, we have found that the chloride compound exhibits a notable broadband PL emission (peak centered at 407 nm, fwhm ~195 nm) in comparison with the bromide compound (peak centered at 438 nm, fwhm ~70 nm). To rationalize this observed broadband PL emission of the chloride hybrid, we have analyzed, in detail, the structural distortion of $[PbX_6]$ octahedra in both structures. As discussed above, both compounds display a large distortion of the $[PbX_6]$ octahedra, but it is different for Cl and Br hybrids. To quantify the octahedral distortion Δd, on the basis of the Pb-X bond lengths, we have used the expression[52,53]

$$\Delta d = \left(\frac{1}{6}\right)\sum\left[\frac{d_n - d}{d}\right]^2$$

where d is the mean Pb−X distance and d_n is the six individual Pb−X distances. The obtained values show that the chloride compound has a very high distortion (Δd ranging from 35.82 × 10^{-4} to 22.37 × 10^{-4}) at room temperature. Nevertheless, the bromide one is less distorted (Δd ranging from 24.97 × 10^{-4} to 17.87 × 10^{-4}). Therefore, a higher distortion and higher difference between the less and the high distorted octahedra seem to be responsible of the unexpected broadband emission of the chloride compound.

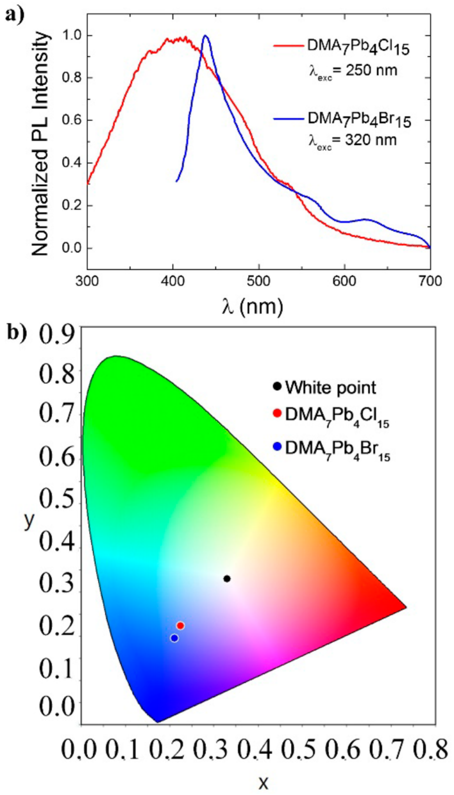

Figure 6. (a) PL spectra of $DMA_7Pb_4X_{15}$ (X = Cl (red) and Br (blue)) at room temperature. (b) Chromaticity coordinates of $DMA_7Pb_4X_{15}$ (X = Cl (red) and Br (blue)) in a 1931 color space chromaticity diagram.

It is worthwhile to note that the PL spectra also shows some anomalies from 500 to 700 nm, which can be due to sub-band gap states.

Finally, the chromaticity coordinates of the obtained halides are plotted in Figure 6b, using the 1931 color space chromaticity diagram. $DMA_7Pb_4Cl_{15}$ has chromaticity coordinates of (0.22, 0.22) whereas $DMA_7Pb_4Br_{15}$ coordinates are (0.21, 0.19), clearly showing that both materials display a similar blue fluorescence.

■ CONCLUSIONS

We have prepared two new lead halides with a general formula of $DMA_7Pb_4X_{15}$ (X = Cl or Br), that are based on the $APbX_3$ photovoltaic hybrid perovskite, and have novel compositions and crystal structures. These new halides were prepared with an easy route and under mild conditions at ambient temperature.

Their crystal structures contain single-layered lead halide frameworks with intercalated DMA cations. Such frameworks display a peculiar arrangement, where linear $[Pb_4X_{15}]^{7-}$ chains are linked to each other and are forming layers. Those $[Pb_4X_{15}]^{7-}$ chains are formed by $[PbX_6]$ distorted octahedra, which are linked to each other through corners and/or faces. Six DMA cations of the asymmetric unit are located between the layers, while the seventh occupies a cavity of the $[Pb_4X_{15}]^{7-}$ framework layer. The DMA cations display a thermally induced order−disorder process, with all of them ordered in the low temperature structure (at 100 K), while several of them are disordered at higher temperatures (at around 275 K). This order−disorder process gives rise to the dielectric transitions observed in both Cl- and Br-hybrids. Such a transition is more acute and takes place at a higher temperature in the case of the Cl-one, as also expected from the DSC results.

Very interestingly, the chloride compound displays a broadband PL emission (peak centered at 407 nm, fwhm ∼195 nm) in comparison with the bromide compound (peak centered at 438 nm, fwhm ∼70 nm). This peculiar broadband is explained on the basis of the $[PbX_6]$ octahedral distortions, which are clearly larger in the chloride hybrid than in the bromide one.

Finally, it is worthwhile to highlight that as the use of the midsize DMA cations allow to prepare a novel family of $A_7Pb_4X_{15}$ lead halides, we anticipate that this novel formula can be adequate to prepare a larger family of compounds with other alkylammonium cations typically used for other hybrid lead halides, such as methylammonium, formamidinium, or ethylammonium. In addition, we suggest that the Pb^{2+} cation can be substituted by another divalent cation (such as Sn^{2+}, Ge^{2+}, Mn^{2+}, etc.). These materials open a novel playground for an easy modulation of electrical and optical properties of new organic−inorganic hybrid materials.

■ ASSOCIATED CONTENT

Ⓢ Supporting Information

The Supporting Information is available free of charge on the ACS Publications website at DOI: 10.1021/acs.inorgchem.7b03217.

> Le Bail refinement of the PXRD data obtained at room temperature, thermogravimetric curves, additional crystallographic figures and tables, and crystallographic files for $DMA_7Pb_4X_{15}$ (X= Cl, Br), CCDC: 1812870; $DMA_7Pb_4Cl_{15}$ (100 K), CCDC: 1812867; $DMA_7Pb_4Cl_{15}$ (275 K), CCDC: 1812868; $DMA_7Pb_4Br_{15}$ (100 K), CCDC: 1812869; and $DMA_7Pb_4Br_{15}$ (275 K) (PDF)

Accession Codes

CCDC 1812867−1812870 contain the supplementary crystallographic data for this paper. These data can be obtained free of charge via www.ccdc.cam.ac.uk/data_request/cif, or by emailing data_request@ccdc.cam.ac.uk, or by contacting The Cambridge Crystallographic Data Centre, 12 Union Road, Cambridge CB2 1EZ, UK; fax: +44 1223 336033.

■ AUTHOR INFORMATION

Corresponding Authors

*E-mail: alberto.garcia.fernandez.
*E-mail: msanchez@udc.es.

ORCID

Alberto García-Fernández: 0000-0003-1671-9979
Juan Manuel Bermúdez-García: 0000-0001-7381-4409
Manuel Sánchez-Andújar: 0000-0002-3441-0994
María Antonia Señarís-Rodríguez: 0000-0002-0117-6855

Notes

The authors declare no competing financial interest.

■ ACKNOWLEDGMENTS

This work was financially supported by the Ministerio de Economía y Competitividad (MINECO) and EU-FEDER under the project ENE2014-56237-C4-4-R and by Xunta de Galicia under the project GRC2014/042. J.M.B.-G. acknowledges Xunta de Galicia for a Postdoctoral Fellowship.

■ REFERENCES

(1) Kojima, A.; Teshima, K.; Shirai, Y.; Miyasaka, T. Organometal Halide Perovskites as Visible- Light Sensitizers for Photovoltaic Cells. *J. Am. Chem. Soc.* **2009**, *131*, 6050−6051.

(2) Kim, H.-S.; Lee, C.-R.; Im, J.-H.; Lee, K.-B.; Moehl, T.; Marchioro, A.; Moon, S.-J.; Humphry-Baker, R.; Yum, J.-H.; Moser, J. E.; Grätzel, M.; Park, N.-G. Lead Iodide Perovskite Sensitized All-Solid-State Submicron Thin Film Mesoscopic Solar Cell with Efficiency Exceeding 9%. *Sci. Rep.* **2012**, *2*, 591.

(3) Etgar, L.; Gao, P.; Xue, Z.; Peng, Q.; Chandiran, A. K.; Liu, B.; Nazeeruddin, M. K.; Gratzel, M. Mesoscopic $CH_3NH_3PbI_3/TiO_2$ Heterojunction Solar Cells. *J. Am. Chem. Soc.* **2012**, *134*, 17396−17399.

(4) Lee, M. M.; Teuscher, J.; Miyasaka, T.; Murakami, T. N.; Snaith, H. J. Efficient Hybrid Solar Cells Based on Meso-Superstructured Organometal Halide Perovskites. *Science* **2012**, *338*, 643−647.

(5) Yang, W. S.; Noh, J. H.; Jeon, N. J.; Kim, Y. C.; Ryu, S.; Seo, J.; Seok, S. Il. High-Performance Photovoltaic Perovskite Layers Fabricated through Intramolecular Exchange. *Science* **2015**, *348*, 1234−1237.

(6) Park, N.-G.; Grätzel, M.; Miyasaka, T.; Zhu, K.; Emery, K. Towards Stable and Commercially Available Perovskite Solar Cells. *Nat. Energy* **2016**, *1*, 16152.

(7) Ono, L. K.; Juárez-Pérez, E. J.; Qi, Y. Progress on Novel Perovskite Materials and Solar Cells with Mixed Cations and Halide Anions. *ACS Appl. Mater. Interfaces* **2017**, *9*, 30197−30246.

(8) Correa-Baena, J.-P.; Abate, A.; Saliba, M.; Tress, W.; Jesper Jacobsson, T.; Grätzel, M.; Hagfeldt, A. The Rapid Evolution of Highly Efficient Perovskite Solar Cells. *Energy Environ. Sci.* **2017**, *10*, 710−727.

(9) Stoumpos, C. C.; Mao, L.; Malliakas, C. D.; Kanatzidis, M. G. Structure − Band Gap Relationships in Hexagonal Polytypes and Low-Dimensional Structures of Hybrid Tin Iodide Perovskites. *Inorg. Chem.* **2017**, *56*, 56−73.

(10) Li, W.; Wang, Z.; Deschler, F.; Gao, S.; Friend, R. H.; Cheetham, A. K. Chemically Diverse and Multifunctional Hybrid Organic−inorganic Perovskites. *Nat. Rev. Mater.* **2017**, *2*, 16099.

(11) Saparov, B.; Mitzi, D. B. Organic-Inorganic Perovskites: Structural Versatility for Functional Materials Design. *Chem. Rev.* **2016**, *116*, 4558−4596.

(12) Tabuchi, Y.; Asai, K.; Rikukawa, M.; Sanui, K.; Ishigure, K. Preparation and Characterization of Natural Lower Dimensional Layered Perovskite-Type Compounds. *J. Phys. Chem. Solids* **2000**, *61*, 837−845.

(13) Mao, L.; Wu, Y.; Stoumpos, C. C.; Wasielewski, M. R.; Kanatzidis, M. G. White-Light Emission and Structural Distortion in New Corrugated Two-Dimensional Lead Bromide Perovskites. *J. Am. Chem. Soc.* **2017**, *139*, 5210−5215.

(14) Pedesseau, L.; Sapori, D.; Traore, B.; Robles, R.; Fang, H. H.; Loi, M. A.; Tsai, H.; Nie, W.; Blancon, J. C.; Neukirch, A.; Tretiak, S.; Mohite, A. D.; Katan, C.; Even, J.; Kepenekian, M. Advances and Promises of Layered Halide Hybrid Perovskite Semiconductors. *ACS Nano* **2016**, *10*, 9776−9786.

(15) Smith, M. D.; Jaffe, A.; Dohner, E. R.; Lindenberg, A. M.; Karunadasa, H. I. Structural Origins of Broadband Emission from Layered Pb−Br Hybrid Perovskites. *Chem. Sci.* **2017**, *8*, 4497−4504.

(16) Becker, M.; Klüner, T.; Wark, M. Formation of Hybrid ABX $_3$ Perovskite Compounds for Solar Cell Application: First-Principles Calculations of Effective Ionic Radii and Determination of Tolerance Factors. *Dalt. Trans.* **2017**, *46*, 3500−3509.

(17) Smith, I. C.; Hoke, E. T.; Solis-Ibarra, D.; McGehee, M. D.; Karunadasa, H. I. A Layered Hybrid Perovskite Solar-Cell Absorber with Enhanced Moisture Stability. *Angew. Chem., Int. Ed.* **2014**, *53*, 11232−11235.

(18) Cao, D. H.; Stoumpos, C. C.; Farha, O. K.; Hupp, J. T.; Kanatzidis, M. G. 2D Homologous Perovskites as Light-Absorbing Materials for Solar Cell Applications. *J. Am. Chem. Soc.* **2015**, *137*, 7843−7850.

(19) Liao, J.-F.; Rao, H.-S.; Chen, B.-X.; Kuang, D.-B.; Su, C.-Y. Dimension Engineering on Cesium Lead Iodide for Efficient and Stable Perovskite Solar Cells. *J. Mater. Chem. A* **2017**, *5*, 2066−2072.

(20) Koh, T. M.; Shanmugam, V.; Schlipf, J.; Oesinghaus, L.; Müller-Buschbaum, P.; Ramakrishnan, N.; Swamy, V.; Mathews, N.; Boix, P. P.; Mhaisalkar, S. G. Nanostructuring Mixed-Dimensional Perovskites: A Route Toward Tunable, Efficient Photovoltaics. *Adv. Mater.* **2016**, *28*, 3653−3661.

(21) Ishihara, T. Optical Properties of PbI-Based Perovskite Structures. *J. Lumin.* **1994**, *60−61*, 269−274.

(22) Tathavadekar, M.; Krishnamurthy, S.; Banerjee, A.; Nagane, S.; Gawli, Y.; Suryawanshi, A. B.; Bhat, S. K.; Puthusseri, D.; Mohite, A.; Ogale, S. Low-Dimensional Hybrid Perovskites as High Performance Anodes for Alkali-Ion Batteries. *J. Mater. Chem. A* **2017**, *5*, 18634−18642.

(23) Mao, L.; Wu, Y.; Stoumpos, C. C.; Traore, B.; Katan, C.; Even, J.; Wasielewski, M. R.; Kanatzidis, M. G. Tunable White-Light Emission in Single-Cation-Templated Three-Layered 2D Perovskites $(CH_3CH_2NH_3)_4Pb_3Br_{10-x}Cl_x$. *J. Am. Chem. Soc.* **2017**, *139*, 11956−11963.

(24) Yuan, Z.; Zhou, C.; Tian, Y.; Shu, Y.; Messier, J.; Wang, J. C.; van de Burgt, L. J.; Kountouriotis, K.; Xin, Y.; Holt, E.; Schanze, K.; Clark, R.; Siegrist, T.; Ma, B. One-Dimensional Organic Lead Halide Perovskites with Efficient Bluish White-Light Emission. *Nat. Commun.* **2017**, *8*, 14051.

(25) Stoumpos, C. C.; Soe, C. M. M.; Tsai, H.; Nie, W.; Blancon, J. C.; Cao, D. H.; Liu, F.; Traoré, B.; Katan, C.; Even, J.; Mohite, A. D.; Kanatzidis, M. G. High Members of the 2D Ruddlesden-Popper Halide Perovskites: Synthesis, Optical Properties, and Solar Cells of $(CH_3(CH_2)_3NH_3)_2(CH_3NH_3)_4Pb_5I_{16}$. *Chem.* **2017**, *2*, 427−440.

(26) Mousdis, G. A.; Gionis, V.; Papavassiliou, G. C.; Raptopoulou, C. P.; Terzis, A. Preparation, Structure and Optical Properties of $[CH_3SC(NH_2)NH_2]_3PbI_5$, $[CH_3SC(NH_2)NH_2]_4Pb_2Br_8$ and $[CH_3SC^-(NH_2)NH_2]_3PbCl_5*CH_3SC(NH_2)NH_2Cl$. *J. Mater. Chem.* **1998**, *8*, 2259−2262.

(27) Yuan, M.; Quan, L. N.; Comin, R.; Walters, G.; Sabatini, R.; Voznyy, O.; Hoogland, S.; Zhao, Y.; Beauregard, E. M.; Kanjanaboos, P.; Lu, Z.; Kim, D. H.; Sargent, E. H. Perovskite Energy Funnels for Efficient Light-Emitting Diodes. *Nat. Nanotechnol.* **2016**, *11*, 872−877.

(28) Dohner, E. R.; Jaffe, A.; Bradshaw, L. R.; Karunadasa, H. I. Intrinsic White-Light Emission from Layered Hybrid Perovskites. *J. Am. Chem. Soc.* **2014**, *136*, 13154−13157.

(29) Yangui, A.; Garrot, D.; Lauret, J. S.; Lusson, A.; Bouchez, G.; Deleporte, E.; Pillet, S.; Bendeif, E. E.; Castro, M.; Triki, S.; Abid, Y.; Boukheddaden, K. Optical Investigation of Broadband White-Light Emission in Self-Assembled Organic-Inorganic Perovskite $(C_6H_{11}NH_3)_2PbBr_4$. *J. Phys. Chem. C* **2015**, *119*, 23638−23647.

(30) Congreve, D. N.; Weidman, M. C.; Seitz, M.; Paritmongkol, W.; Dahod, N. S.; Tisdale, W. A. Tunable Light-Emitting Diodes Utilizing Quantum-Confined Layered Perovskite Emitters. *ACS Photonics* **2017**, *4*, 476−481.

(31) McCall, K. M.; Stoumpos, C. C.; Kostina, S. S.; Kanatzidis, M. G.; Wessels, B. W. Strong Electron-Phonon Coupling and Self-Trapped Excitons in the Defect Halide Perovskites $A_3M_2I_9$ (A = Cs, Rb; M = Bi, Sb). *Chem. Mater.* **2017**, *29*, 4129−4145.

(32) Hu, T.; Smith, M. D.; Dohner, E. R.; Sher, M. J.; Wu, X.; Trinh, M. T.; Fisher, A.; Corbett, J.; Zhu, X. Y.; Karunadasa, H. I.; Lindenberg, A. M. Mechanism for Broadband White-Light Emission from Two-Dimensional (110) Hybrid Perovskites. *J. Phys. Chem. Lett.* **2016**, *7*, 2258−2263.

(33) Knutson, J. L.; Martin, J. D.; Mitzi, D. B. Tuning the Band Gap in Hybrid Tin Iodide Perovskite Semiconductors Using Structural Templating. *Inorg. Chem.* **2005**, *44*, 4699−4705.

(34) Amat, A.; Mosconi, E.; Ronca, E.; Quarti, C.; Umari, P.; Nazeeruddin, M. K.; Grätzel, M.; De Angelis, F. Cation-Induced Band-Gap Tuning in Organohalide Perovskites: Interplay of Spin-Orbit Coupling and Octahedra Tilting. *Nano Lett.* **2014**, *14*, 3608−3616.

(35) Cortecchia, D.; Neutzner, S.; Kandada, A. R. S.; Mosconi, E.; Meggiolaro, D.; De Angelis, F.; Soci, C.; Petrozza, A. Broadband

Emission in Two-Dimensional Hybrid Perovskites: The Role of Structural Deformation. *J. Am. Chem. Soc.* **2017**, *139*, 39−42.

(36) Stoumpos, C. C.; Cao, D. H.; Clark, D. J.; Young, J.; Rondinelli, J. M.; Jang, J. I.; Hupp, J. T.; Kanatzidis, M. G. Ruddlesden-Popper Hybrid Lead Iodide Perovskite 2D Homologous Semiconductors. *Chem. Mater.* **2016**, *28*, 2852−2867.

(37) Zhang, W.; Xiong, R. G. Ferroelectric Metal-Organic Frameworks. *Chem. Rev.* **2012**, *112*, 1163−1195.

(38) Mączka, M.; Gągor, A.; Macalik, B.; Pikul, A.; Ptak, M.; Hanuza, J. Order−Disorder Transition and Weak Ferromagnetism in the Perovskite Metal Formate Frameworks of $[(CH_3)_2NH_2][M(HCOO)_3]$ and $[(CH_3)_2ND_2][M(HCOO)_3]$ (M = Ni, Mn). *Inorg. Chem.* **2014**, *53*, 457−467.

(39) Jain, P.; Dalal, N. S.; Toby, B. H.; Kroto, H. W.; Cheetham, A. K. Order-Disorder Antiferroelectric Phase Transition in a Hybrid Inorganic-Organic Framework with the Perovskite Architecture. *J. Am. Chem. Soc.* **2008**, *130*, 10450−10451.

(40) Sánchez-Andújar, M.; Presedo, S.; Yañez-Vilar, S.; Castro-García, S.; Shamir, J.; Senaris-Rodriguez, M. A. Characterization of the Order-Disorder Dielectric Transition in the Hybrid Organic-Inorganic Perovskite-like Formate $Mn(HCOO)_3[(CH_3)_2NH_2]$. *Inorg. Chem.* **2010**, *49*, 1510−1516.

(41) Zhang, W.; Ye, H. Y.; Graf, R.; Spiess, H. W.; Yao, Y. F.; Zhu, R. Q.; Xiong, R. G. Tunable and Switchable Dielectric Constant in an Amphidynamic Crystal. *J. Am. Chem. Soc.* **2013**, *135*, 5230−5233.

(42) García-Fernández, A.; Bermúdez-García, J. M.; Castro-García, S.; Llamas-Saiz, A. L.; Artiaga, R.; López-Beceiro, J.; Hu, S.; Ren, W.; Stroppa, A.; Sánchez-Andújar, M.; Señarís-Rodríguez, M. A. Phase Transition, Dielectric Properties, and Ionic Transport in the $[(CH_3)_2NH_2]PbI_3$ Organic-Inorganic Hybrid with 2H-Hexagonal Perovskite Structure. *Inorg. Chem.* **2017**, *56*, 4918−4927.

(43) Larson, A. C.; Von Dreele, R. B. *General Structure Analysis System (GSAS)*; Los Alamos National Laboratories, 1990; pp 86−748.

(44) Toby, B. H. EXPGUI, a Graphical User Interface for GSAS. *J. Appl. Crystallogr.* **2001**, *34*, 210−213.

(45) Sheldrick, G. M. Crystal Structure Refinement with SHELXL. *Acta Crystallogr., Sect. C: Struct. Chem.* **2015**, *71*, 3−8.

(46) Kortüm, G.; Braun, W.; Herzog, G. Principles and Techniques of Diffuse-Reflectance Spectroscopy. *Angew. Chem., Int. Ed. Engl.* **1963**, *2*, 333−341.

(47) *OSRAM SYLVANIA*. LED ColorCalculator, https://www.osram.us/cb/tools-and-resources/applications/led-colorcalculator/index.jsp.

(48) Sánchez-Andújar, M.; Gómez-Aguirre, L. C.; Pato Doldán, B.; Yáñez-Vilar, S.; Artiaga, R.; Llamas-Saiz, A. L.; Manna, R. S.; Schnelle, F.; Lang, M.; Ritter, F.; Haghighirad, A. A.; Señarís-Rodríguez, M. A. First-Order Structural Transition in the Multiferroic Perovskite-like Formate $[(CH_3)_2NH_2][Mn(HCOO)_3]$. *CrystEngComm* **2014**, *16*, 3558−3566.

(49) Bermúdez-García, J. M.; Sánchez-Andújar, M.; Señarís-Rodríguez, M. A. A New Playground for Organic−Inorganic Hybrids: Barocaloric Materials for Pressure-Induced Solid-State Cooling. *J. Phys. Chem. Lett.* **2017**, *8*, 4419−4423.

(50) Kumawat, N. K.; Dey, A.; Kumar, A.; Gopinathan, S. P.; Narasimhan, K. L.; Kabra, D. Band Gap Tuning of $CH_3NH_3Pb(Br_{1-x}Cl_x)$ Hybrid Perovskite for Blue Electroluminescence. *ACS Appl. Mater. Interfaces* **2015**, *7*, 13119−13124.

(51) Takagi, H.; Kunugita, H.; Ema, K. Influence of the Image Charge Effect on Excitonic Energy Structure in Organic-Inorganic Multiple Quantum Well Crystals. *Phys. Rev. B: Condens. Matter Mater. Phys.* **2013**, *87*, 1−5.

(52) Katan, C.; Pedesseau, L.; Kepenekian, M.; Rolland, A.; Even, J. Interplay of Spin−orbit Coupling and Lattice Distortion in Metal Substituted 3D Tri-Chloride Hybrid Perovskites. *J. Mater. Chem. A* **2015**, *3*, 9232−9240.

(53) Lufaso, M. W.; Woodward, P. M. Jahn-Teller Distortions, Cation Ordering and Octahedral Tilting in Perovskites. *Acta Crystallogr., Sect. B: Struct. Sci.* **2004**, *60*, 10−20.

DOI: 10.1021/acs.inorgchem.7b03217